A Fundamental Study of Boron Deposition and Poisoning of $La_{0.8}Sr_{0.2}MnO_3$ Cathode of Solid Oxide Fuel Cells under Accelerated Conditions

Kongfa Chen,[a] Shu-Sheng Liu,[b,c] Paul Guagliardo,[d] Matt R. Kilburn,[d] Michihisa Koyama,[b,c,e,*,z] and San Ping Jiang[a,z]

[a]*Fuels and Energy Technology Institute & Department of Chemical Engineering, Curtin University, Perth, WA 6102, Australia*
[b]*INAMORI Frontier Research Center, Kyushu University, Fukuoka 819-0395, Japan*
[c]*CREST, Japan Science and Technology Agency, Tokyo 102-0076, Japan*
[d]*Centre for Microscopy, Characterisation and Analysis, The University of Western Australia, Clawley, WA 6009, Australia*
[e]*International Institute for Carbon-Neutral Energy Research, Kyushu University, Fukuoka 819-0395, Japan*

Borosilicate glass and glass-ceramics are the most common sealant materials for planar solid oxide fuel cells (SOFCs). This study focuses on the fundamentals of deposition and poisoning of volatile boron species from the borosilicate glass on the electrocatalytic activity and microstructure of $La_{0.8}Sr_{0.2}MnO_3$ (LSM) cathodes under accelerated SOFC operation conditions, using EIS, SEM, FIB-SEM, HRTEM, NanoSIMS, XPS and ICP-OES. The presence of boron species poisons and deteriorates the electrochemical activity and stability for the O_2 reduction reaction on the LSM cathodes. Boron deposition occurs randomly on the LSM electrode surface under open circuit but is driven to the electrode/electrolyte interface region under cathodic polarization conditions, resulting in the formation of $LaBO_3$ and Mn_2O_3 and the disintegration of the LSM perovskite structure. The preferential boron deposition at the interface is most likely due to the increased activity of the highly energetic lanthanum at LSM lattice sites at the three phase boundary region under cathodic polarization conditions, accelerating the reaction rate between the gaseous boron species and energetic La. This study provides a fundamental insight into the boron deposition and its interaction with SOFC cathodes.
 [DOI: 10.1149/2.0141512jes]

Manuscript submitted June 17, 2015; revised manuscript received August 12, 2015. Published August 21, 2015.

Solid oxide fuel cells (SOFCs) are an energy conversion device to directly transfer the chemical energy of fuels to electrical energy, and are the most efficient and least polluting energy conversion technology among various kinds of fuel cells. One critical issue of the development of reliable and durable SOFCs is the gradual degradation of activity at the cathode side during long-term operation, due to the attack by volatile impurities such as chromium from the Fe-Cr interconnect, sulfur from the air stream and boron from borosilicate-based glass sealants.[1–3]

Borosilicate glass and glass-ceramic materials are the most common sealants to seal the edge of planar SOFCs to hermetically separate fuels supplied to the anode and air to the cathode.[4–9] The sealing and thermomechanical properties and the compatibility and interface between glass-ceramic sealant materials, metallic interconnect and electrolyte have been extensively studied.[8,10–14] However, under the SOFC operation condition boron species from the borosilicate glass are highly volatile to form BO_2 under dry conditions and $B_3H_3O_6$ under wet, reducing conditions.[2,15] Earlier studies show that volatile species from glass sealants can significantly affect the microstructure of LSM electrodes.[16] Komatsu et al.[17] used glass to seal an anode-supported planar cell and found that the concentration of boron in the cathode exhaust gas trapped by a water condenser increased with the operation time during the long-term test at 800°C for 6500 h. We recently carried out a series of detailed studies on the effect of boron poisoning on electrode performance of the most common $(La,Sr)MnO_3$ (LSM), $(La,Sr)(Co,Fe)O_3$ (LSCF) and $(Ba,Sr)(Co,Fe)O_3$ (BSCF) cathodes, by heat-treating the electrodes in the presence of borosilicate glass.[18–21] Boron is chemically incompatible with the cathode materials, and preferentially reacts with the A-site cations in particular lanthanum to form insulating lanthanum borate, $LaBO_3$.[22] The reaction between boron and LSM to form $LaBO_3$ is generally slow under open circuit conditions.[19] On the other hand, boron has a substantially higher reactivity with the LSCF under the identical heat-treatment conditions and the reaction results in the decomposition of the LSCF structure and the formation of $LaBO_3$ and Fe_2O_3.[20] Compared to LSCF, La-free BSCF cathode is more resistant to boron poisoning. Boron deposition mainly occurs in the outmost electrode layer of the BSCF cathode, while the inner region close to the electrode/electrolyte interface is relatively intact and still functions electrochemically.[21] This indicates that boron deposition and poisoning is closely related to the composition of the SOFC cathode materials.

The deposition and poisoning of boron impurities on SOFC cathodes could also be affected by the operation conditions. Zhou et al. polarized LSM-YSZ and LSCF cathodes at a cell voltage of 0.7 V with boron partial pressure of $\sim 10^{-9}$ atm for 150 h, and reported boron deposition in both the cathodes with a content of ~500 ppm in LSCF and ~40 ppm in LSM-YSZ at 750°C.[2] On the other hand, our recent study has shown that for the O_2 reduction reaction on LSCF electrodes under cathodic polarization, boron deposition occurs preferentially within a certain depth of the electrode/electrolyte interface region e.g. 6 μm in the case of a 28 μm-thick electrode and 2.5 μm in the case of a 6 μm-thick electrode.[23] However, the mechanism of boron poisoning and its influence on the microstructure and electrochemical activity of LSM electrodes under SOFC operation conditions have not been fully understood.

In practical planar SOFCs, glass sealants are generally used on the edge of the cells to seal the interface between the cathode and metallic interconnect (see Scheme 1a). The contact between the sealant materials and cathode can be very small or minimum and volatile boron species could only escape from the edge of the sealant. Thus, boron deposition and poisoning process is generally slow. This is very different from the significant Cr deposition and poisoning effect of the metallic interconnect due to the face-to-face contact between the metallic interconnect and cathodes. This is also probably the reason for the much less attention on this important issue. However, under long-term SOFC operation conditions, volatile boron species can accumulate on the cathode side of SOFC stacks, leading to the irreversible performance degradation.[17] Therefore, it is important to fundamentally understand the detrimental effect of boron species on the performance degradation of cathodes under SOFC operation conditions. In this study, we accelerate the boron deposition and poisoning process by placing a borosilicate glass pellet on top of cathodes,

*Electrochemical Society Active Member.
[z]E-mail: koyama@ifrc.kyushu-u.ac.jp; s.jiang@curtin.edu.au

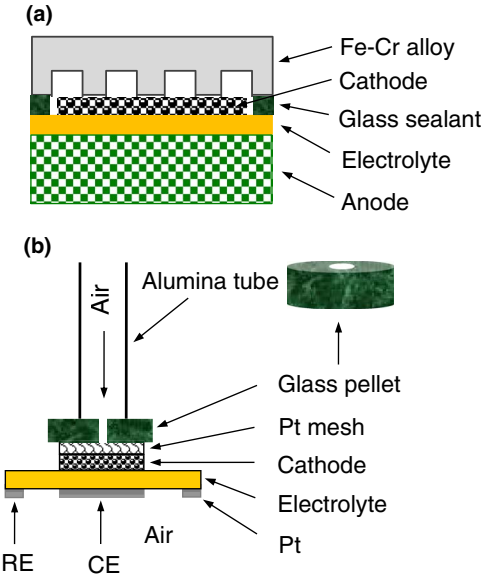

Scheme 1. Schematic diagram of (a) a typical planar SOFC with the edge sealed by the borosilicate glass sealant and (b) setup for the investigation of boron deposition and poisoning of cathodes under acceleration conditions. In (b) Pt mesh is used as the buffer layer to avoid the direct contact between borosilicate glass and cathode.

similar to that used in the chromium studies.[24] The direct contact between glass and cathode is avoided by using a platinum mesh as the buffer layer (Scheme 1b). In this way volatile boron species can only deposit on the cathode via gas phase diffusion. The electrode activity and stability of LSM cathode are investigated in the presence of borosilicate glass under open circuit and cathodic polarization operation conditions. The results show that boron deposition is related to the activity of lanthanum at the LSM lattice, which in turn is related to the O_2 reduction reaction at the electrode/electrolyte interface region.

Experimental

Electrode preparation and testing.— $La_{0.8}Sr_{0.2}MnO_3$ (LSM, Fuel Cell Materials) cathodes were prepared on dense 8 mol% Y_2O_3 stabilized ZrO_2 (YSZ, Tosoh, Japan) electrolyte pellets. The electrolyte pellets were prepared by die pressing YSZ powder and sintering at 1450°C for 4 h. The pellets were 0.8–0.9 mm in thickness and 18 mm in diameter. LSM was applied onto the YSZ pellets by slurry coating and sintered at 1150°C for 3 h. The thickness of the LSM electrode was 20–30 μm, and the electrode surface area was 0.5 cm^2. Borosilicate glass powder (70% SiO_2, 10% B_2O_3, 8% Na_2O, 8% K_2O and 1% CaO) was used as the source of boron. The composition of glass with 10% boron is typically used as glass sealant materials as reported in the literature.[25] The glass powder was pre-sintered into pellets with a hole in the center and heat-treated at 800°C for 2 h. The pellet was ~4.0 mm in thickness and ~9 mm in diameter, and the diameter of the central hole was 1.6 mm. The glass pellet was placed on top of the cathode separated with a Pt mesh to avoid direct contact between the cathode and glass pellet (see Scheme 1b).

Electrochemical tests were carried out using a three-electrode method with Pt (Gwent Electronic Materials Ltd) as the counter and reference electrodes, respectively. Polarization performance and electrochemical impedance responses were measured using a Gamry Reference 3000 Potentiostat. Electrochemical impedance curves were recorded under open circuit conditions in the frequency range from 0.1 Hz to 100 kHz with a signal amplitude of 10 mV. Electrode ohmic resistance (R_Ω) was obtained from the high frequency intercept, and electrode polarization resistance (R_E) was measured by the differences between the high and low frequency intercepts. For comparison, the electrochemical performance of LSM electrodes was also measured in the absence of glass pellet. At least two identical samples were measured to ensure the reproducibility. LSM bar samples were also prepared by die compaction at 110 MPa, densifying at 1350°C in air for 5 h, and followed by the heat-treatment in a quartz tube in the presence of borosilicate glass powder at 800°C in dry air for 30 days.[26]

To investigate the catalytic activity of possible borate and oxides formed during the boron poisoning process, we used a well-defined thin Pt electrode as the model skeleton[27] to infiltrate lanthanum borate, strontium borate and manganese oxide. The Pt skeleton was prepared on a YSZ electrolyte by slurry coating, and sintered at 1050°C for 2 h. La, Sr and Mn nitrate-boric acid aqueous solutions of 0.2 mol L^{-1} were prepared from $La(NO_3)_3 \cdot 6H_2O$ (99.9%, Alfa-Aesar), $Sr(NO_3)_2$ (99%, Sigma-Aldrich), $Mn(NO_3)_2$ (50 wt% solution, Alfa-Aesar), and H_3BO_3 (≥99.5%, Sigma-Aldrich). The solution was infiltrated into the Pt skeleton and heat-treated at 800°C for 2 h.

Characterization.— LSM electrodes after the electrochemical tests were dissolved by 3 M HCl (diluted from 30% HCl, Suprapur, Merck KGaA, Darmstadt, Germany) and the composition was analyzed using inductively coupled plasma optical emission spectrometry (Optima DV 7300 ICP-OES, PerkinElmer). The phase of LSM was characterized by X-ray diffractometry (Bruker D8 Advance). X-ray photoelectron spectroscopy (XPS) was carried out using a Kratos AXIS Ultra DLD system, with monochromated Al Kα X-rays (photon energy 1486.7 eV), a 110 μm aperture and a pass energy of 20 eV. The XPS spectra were calibrated by C 1s peak at 284.8 eV.

The microstructure of the cathodes was examined using scanning electron microscopy (SEM, Zeiss Neon 40EsB). For the LSM cathode after polarization at 200 mA cm^{-2} for 100 h in the presence of borosilicate glass, epoxy resin was infiltrated under vacuum. A thin wafer sample was lifted out in a focused ion beam-SEM (FIB-SEM, FEI Quanta 200i 3D) and polished in another FIB-SEM (HITACHI MI4000L). Microstructure observation and elemental mapping analysis of the wafer sample were carried out using both HITACHI MI4000L and scanning/high-resolution transmission electron microscopy (STEM/HRTEM, JEOL JEM-ARM200F, 200 kV) equipped with energy dispersive X-ray spectroscopy (EDS) detectors. Elemental mapping was carried out using the CAMECA NanoSIMS 50. All measurements were performed with an O^- primary beam, with a spot size of approximately 400 nm, impact energy of 16 keV, and a beam current of 6 pA. A 10 nm thick gold coating was applied to the samples to provide conductivity. The instrument was operated in multicollector mode, allowing the simultaneous detection of five ion species from the same analysis region. Prior to imaging, the sample surface was presputtered with the primary ion beam to achieve an ion dose $> 1 \times 10^{17}$ ions cm^{-2}, in order to remove surface contamination and implant O^- ions to reach a steady-state of ion emission. Secondary ion images were obtained by rastering the primary ion beam across areas measuring 30–50 μm,[2] at a resolution of 256 × 256 pixels, with dwell times of 90 ms per pixel.

Results and Discussion

Electrochemical performance.— Figure 1 shows the impedance responses and polarization curves of LSM cathodes as a function of cathodic current passage time at 200 mA cm^{-2} and 800°C for 100 h. For the polarization in the absence of borosilicate glass, the initial overpotential (η) was 0.35 V and dropped rapidly to 0.17 V after polarization for 1 h, followed by a gradual decrease and reached 0.10 V after polarization for 100 h (Fig. 1a). The initial R_E was 6.6 Ω cm^2, and decreased to 2.5 and 1.0 Ω cm^2 after polarization at 200 mA cm^{-2} for 5 min and 100 h, respectively (Fig. 1b). The significant reduction in η and R_E is due to the activation effect of cathodic polarization on the electrochemical activity of LSM electrodes.[28] For the O_2 reduction reaction in the presence of borosilicate glass, the initial η and R_E were 0.52 V and 23.3 Ω cm^2 (Figs. 1c and 1d), respectively, higher than 0.35 V and 6.6 Ω cm^2 in the absence of borosilicate glass. This indicates that the electrode activity of LSM electrode was deteriorated in the presence of borosilicate glass sealant materials

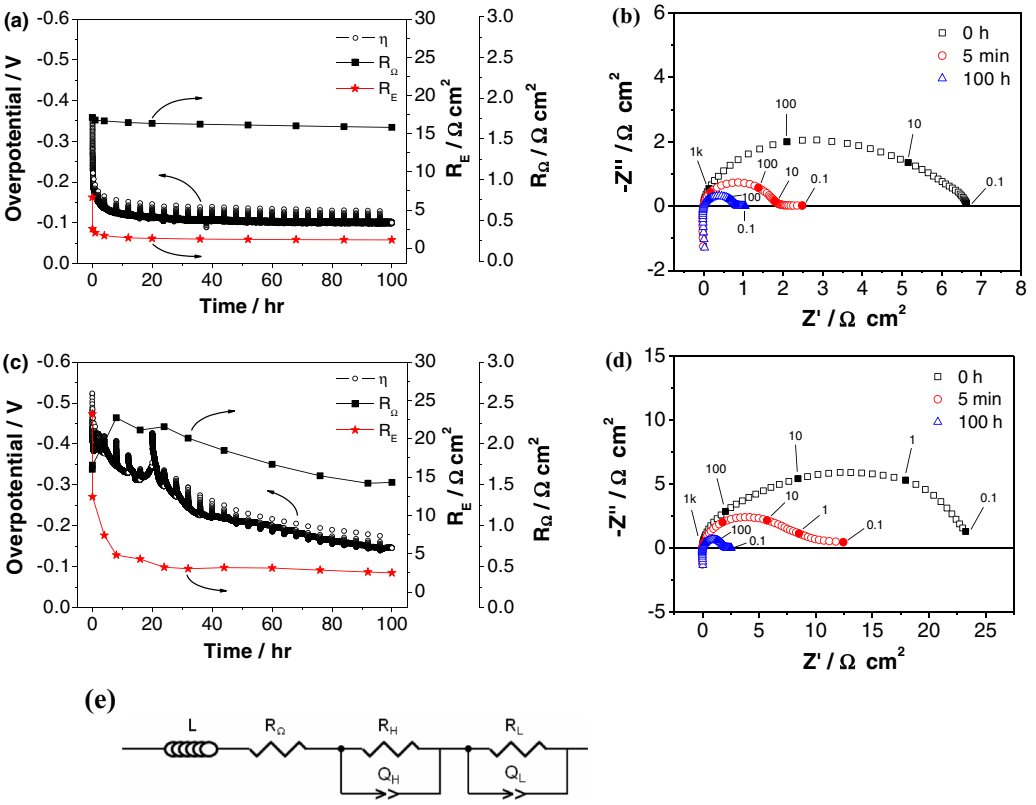

Figure 1. Polarization curves and impedance responses for the O_2 reduction reaction on LSM cathodes under cathodic current passage at 200 mA cm^{-2} and 800°C for 100 h in the (a,b) absence and (c,d) presence of borosilicate glass. Equivalent circuit for the fitting is shown in (e).

during ramping to 800°C. The decrease in η and R_E is much slower in the presence of borosilicate glass. For example, the initial η was 0.52 V and decreased slowly to 0.35 V and 0.15 V after polarization for 8 h and 100 h, respectively (Fig. 1c). The initial R_E was 23.3 Ω cm^2 and decreased to 12.4 and 2.5 Ω cm^2 after polarization for 5 min and 100 h, respectively (Fig. 1d). This indicates that the activation effect of cathodic polarization on LSM electrodes is inhibited in the presence of borosilicate glass.

R_Ω is more or less stable during the cathodic polarization in the absence of borosilicate glass (Fig. 1a). The initial R_Ω was 1.76 Ω cm^2 and changed slightly to 1.64 Ω cm^2 after polarization for 100 h. Different to that in the absence of borosilicate glass, R_Ω changes with the polarization in the presence of borosilicate glass. The initial R_Ω was 1.69 Ω cm^2, reached a maximum of 2.32 Ω cm^2 after polarization for 8 h and then decreased to 1.53 Ω cm^2 after polarization for 100 h (Fig. 1b). This indicates the presence of borosilicate glass also has an effect on the ohmic resistance of the LSM electrodes.

The impedance responses of LSM cathodes are characterized by a depressed arc (Figs. 1b and 1d). Previous studies have shown that there are at least two electrode processes associated with the high and low frequencies (R_H and R_L); the high frequency process is related to the ion migration from the cathode to the electrolyte and the low frequency process is associated with oxygen surface dissociation and diffusion processes.[29,30] The impedance responses were fitted with an equivalent circuit (Fig. 1e). The results show that R_L values were 18.97 and 0.86 Ω cm^2 before and after polarization for 100 h in the presence of borosilicate glass, respectively, significantly higher than 2.84 and 0.17 Ω cm^2 for the reaction in the absence of borosilicate glass under identical polarization conditions. This indicates the poisoning of LSM by boron species is predominantly on the oxygen surface dissociation and diffusion processes.

Figure 2 shows the plots of R_Ω and R_E values and impedance responses of LSM electrodes measured under open circuit conditions in the absence and presence of borosilicate glass at 800°C for 20 h. R_Ω of both electrodes is quite stable during the tests (Fig. 2), which is different to the variation of R_Ω during the polarization in the presence of borosilicate glass (Fig. 1b). For the O_2 reduction reaction in the absence of borosilicate glass, the electrode activity is generally stable during the test. The initial R_E before the test was 4.7 Ω cm^2, and increased slightly to 6.1 Ω cm^2 after the test for 20 h (Figs. 2a and 2b). In the presence of borosilicate glass, the initial R_E was 21.4 Ω cm^2, much greater than 4.7 Ω cm^2 in the absence of borosilicate glass (Figs. 2c and 2d). R_E reached a maximum of 30.4 Ω cm^2 after test for 1 h and decreased gradually to 14.3 Ω cm^2 under open circuit for 20 h. This indicates that under the open circuit conditions volatile boron also poisons the electrocatalytic activity of the LSM electrodes.

Microstructure.— Figure 3 shows the SEM micrographs of LSM cathodes after polarization at 200 mA cm^{-2} and 800°C for 100 h in the absence and presence of borosilicate glass. The electrode structure of as-prepared LSM is characterized by interconnected particles in the size range of 0.3–1.7 μm with smooth surface and the contact between the electrolyte and electrode is good (Figs. 3a and 3b). After polarization at 200 mA cm^{-2} for 100 h in the absence of borosilicate glass, the LSM grains are intact (Figs. 3c and 3d), but there is a clear formation of crystal facets on the surface of LSM grains in direct contact with the electrolyte (indicated by circles, Fig. 3c). For LSM grains in the electrode bulk and on the electrode surface, there is no such crystal facet formation (Figs. 3c and 3d). This implies that the crystal facet formation on LSM grains at the electrode/electrolyte interface is most likely induced by the O_2 reduction reaction, consistent with the early observation of morphology change at the three phase boundaries for the reaction on LSM electrodes.[31] On the other hand, after polarization in the presence of borosilicate glass, a significant microstructural change was observed on the LSM grains within ~1 μm interface region, while beyond the interface region in the electrode bulk the LSM grain surface are clean with very few deposits (Figs. 3e and 3g). LSM grains close to the interface layer were

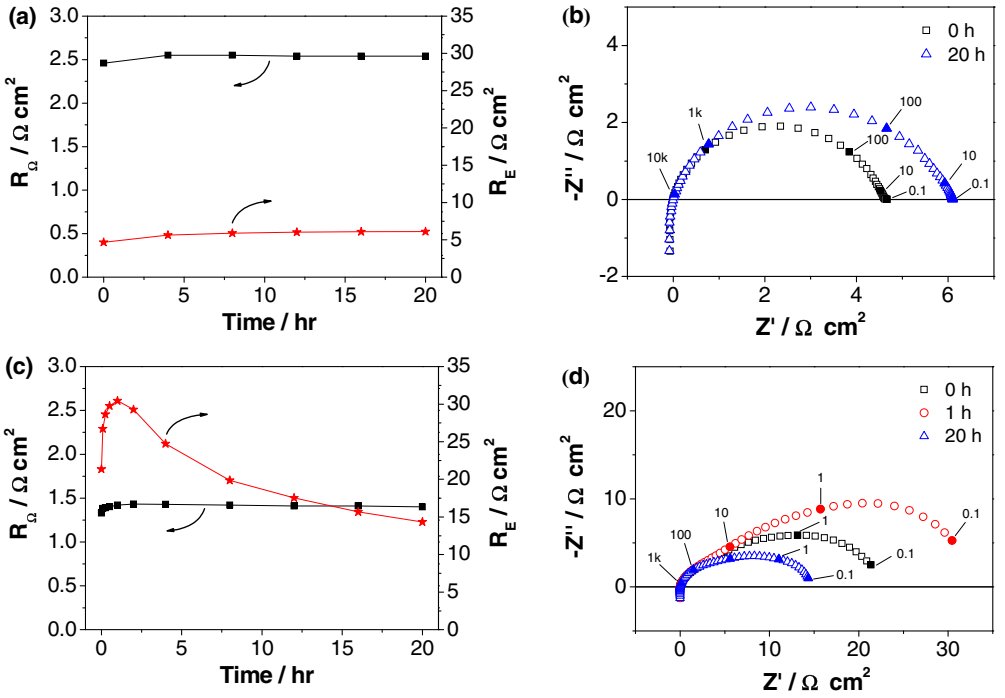

Figure 2. Plots of R_Ω & R_E and impedance responses for the O_2 reduction reaction on LSM cathodes under open circuit conditions at 800°C for 20 h in the (a,b) absence and (c,d) presence of borosilicate glass.

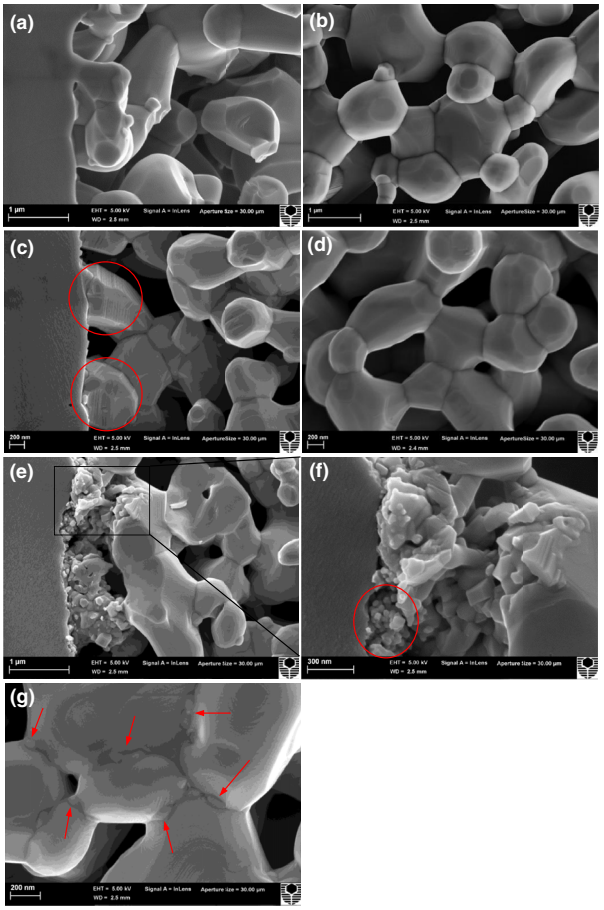

Figure 3. SEM micrographs of cross sections and surface of LSM cathodes: (a,b) as-prepared, and after cathodic current passage at 200 mA cm^{-2} for 100 h in the (c,d) absence and (e, f, g) presence of borosilicate glass.

disintegrated into irregularly shaped particles of 100–240 nm in size on the LSM side, and fine spherical particles of 30–90 nm in size close to the YSZ surface side (indicated by circle, Fig. 3f). On the outer electrode surface fine particles of 70–160 nm in size were formed on the LSM grain boundaries (indicated by the arrows, Fig. 3g). There is no detection of new crystal phase formation on the LSM surface by XRD (results not shown), which confirms that the disintegration of LSM grains occurs mainly at the electrode/electrolyte interface region.

Figure 4 shows the SEM micrographs of the LSM cathode after testing under open circuit conditions in the presence of borosilicate glass for 20 h. In comparison with the smooth and clean surface of as-prepared LSM electrodes (Figs. 3a and 3b), there is significant microstructural change after exposure of the electrode to

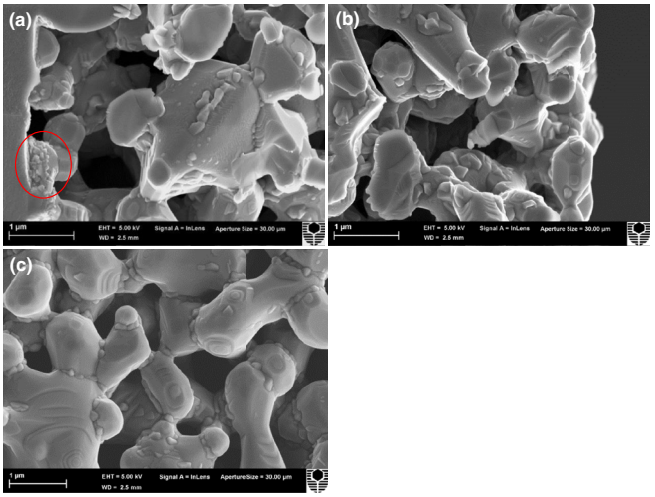

Figure 4. SEM micrographs of (a,b) cross section and (c) surface of a LSM cathode under open circuit at 800°C for 20 h in the presence of borosilicate glass.

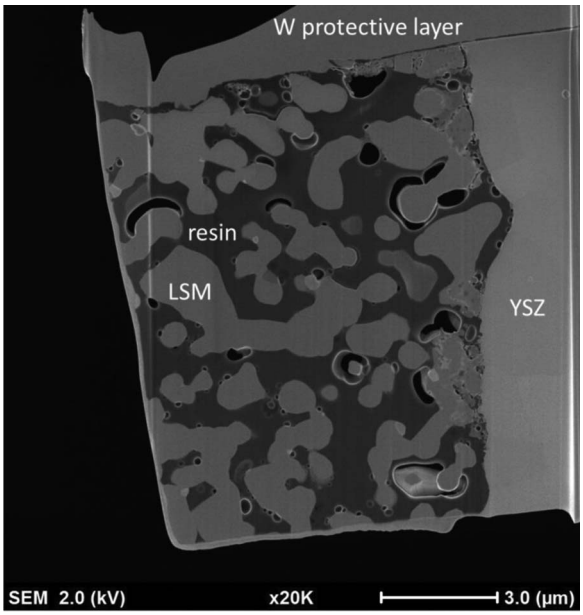

Figure 5. SEM micrograph of a thin wafer sample of a LSM cathode after polarization at 200 mA cm^{-2} for 100 h in the presence borosilicate glass.

boron-containing air under open circuit conditions. There is deposition of large number of fine particles (50–300 nm) with very different morphology to the large LSM particles on the surface of LSM grain. Except a few isolated and fine particles at the electrode interface region (indicated by circle, Fig. 4a), the deposition of fine particles is essentially random in the electrode bulk (Figs. 4a and 4b) and on the electrode surface (Fig. 4c). On the outer electrode surface, the fine deposits are in the LSM grain boundaries as well as on the surface of LSM grains (Fig. 4c). This indicates that boron deposition also occurs on the LSM electrode under open circuit condition, but the effect of boron species or boron deposition is very different from the observed significant microstructural change at the electrode/electrolyte interface region under the influence of cathodic polarization (Fig. 3).

To better elucidate the microstructural changes and the elemental distribution, a thin wafer sample was lifted-out by FIB-SEM from the LSM/YSZ interface region after polarization at 200 mA cm^{-2} and 800°C for 100 h in the presence of borosilicate glass (see Fig. 5). Compared with the dense LSM grains in the bulk of the electrode, the LSM grains at the electrode/electrolyte interface region become disintegrated with the formation of nanoparticles. Fig. 6 shows the EDS maps in the bulk and at the electrode/electrolyte interface region of the wafer sample. La, Sr and Mn cations are uniformly distributed in the bulk of the electrode, but there is also a Mn-O rich spot (indicated by the circles, Fig. 6a). Mn_2O_3 segregation in the LSM electrode during the electrode sintering process at high temperatures has been reported, and the morphology is characterized by dense grains.[32] In the electrode/electrolyte interface region, distinctive Mn-O enrichment (indicated by the circles, Fig. 6b) was also found in the nanoparticle area at the interface. Further analysis on this area by using STEM-EDS is shown in Fig. 7a. A number of nanoparticles together with large agglomerates were observed in the LSM layer close to the YSZ electrolyte. The EDS mapping indicates that these particles are rich in Mn. HRTEM taken on a large Mn-rich particle (indicated by the star, Fig. 7a) identified the [320] zone axis of cubic Mn_2O_3 with the facets of (002) and $(2\bar{3}1)$[33] (Fig. 7b). The d spacing of the (002) and $(2\bar{3}1)$ facets is 0.49 and 0.27 nm, respectively.

Fig. 8a shows the STEM micrograph and EDS maps of a particle within the electrode at the interface. The boron map was not presented because of the poor resolution and its overlapping with Zr. Nevertheless, the EDS maps of other elements clearly show that there is predominant La segregation in the particle close to the electrolyte,

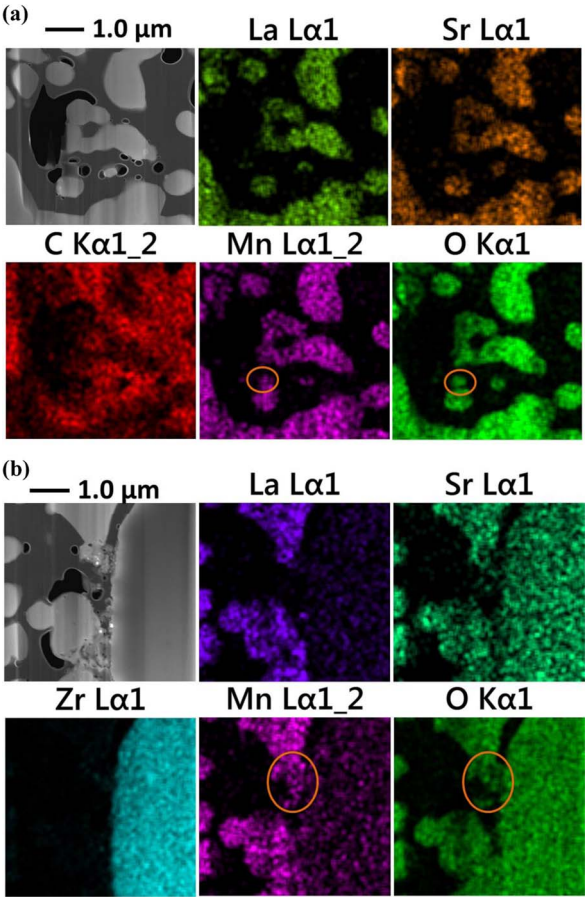

Figure 6. SEM micrographs and EDS elemental maps of the LSM thin wafer sample (a) in the bulk and (b) at the electrode/electrolyte interface. In (b), the appearance of Sr in the YSZ side is due to the overlap of Sr and Y signals.

while Mn-rich nanoparticles were also observed on the La segregated particle surface (indicated by the arrows, Fig. 8a). HRTEM was conducted on a La-rich area (indicted by the star, Fig. 8a) and indicates the existence of an orthorhombic $LaBO_3$ phase, which shows $[0\bar{1}1]$ zone axis with the facets of (111) and $(1\bar{1}\bar{1})$ (Fig. 8b). The d spacing of both the facets is 0.35 nm, close to that of $LaBO_3$ powder.[34]

NanoSIMS, ICP-OES and XPS.— Fig. 9 shows the NanoSIMS images of the LSM cathodes before and after polarization at 200 mA cm^{-2} and 800°C for 100 h. For the LSM polarized in the absence

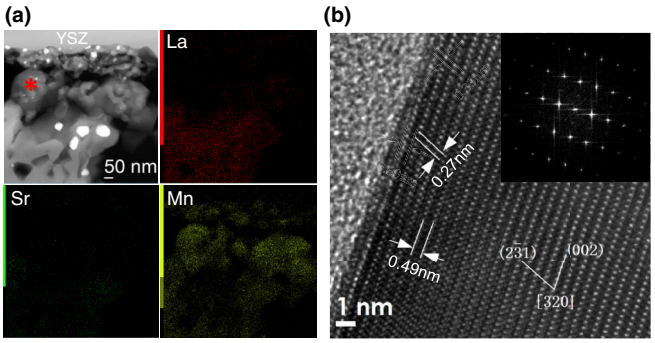

Figure 7. (a) STEM micrograph and EDS elemental maps of the LSM thin wafer sample in a manganese enriched/segregated area and (b) HRTEM micrograph of a Mn rich particle marked by ∗ in (a) and inset is the fast Fourier transform (FFT).

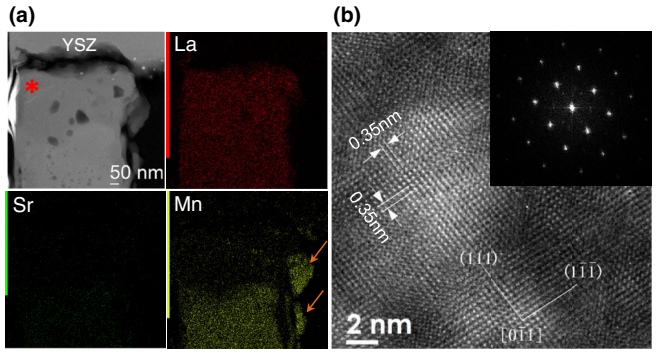

Figure 8. (a) STEM micrograph and EDS elemental maps of the LSM thin wafer sample in a lanthanum enriched/segregated area and (b) HRTEM micrograph of the area marked by ∗ in (a) and inset is the image of fast Fourier transform (FFT).

of borosilicate glass for 100 h, no boron species were detected, as expected, and there are no visible La or Sr segregations either in the bulk of the electrode or at the electrode/electrolyte interface, though there are a few Mn-rich spots in the bulk of the electrodes in both cases (Fig. 9b). The element distribution of the polarized LSM in the absence of borosilicate glass is similar to that of as-prepared LSM (Fig. 9a). After polarization in the presence of borosilicate glass at 200 mA cm^{-2} and 800°C for 100 h, significant boron deposition and lanthanum enrichment are observed at the electrode/electrolyte interface region (Fig. 9c). The thickness of the reaction zone is ∼2 μm. In addition, Mn segregation with a discrete distribution was also observed at the interface region, while Sr cation appears to be moved away from the interface. NanoSIMS analysis of a dense LSM bar sample after heat-treatment at 800°C for 30 days in the presence of borosilicate glass shows boron deposition in the surface region, in addition to the Mn and in particular La enrichment and Sr deficiency on the surface (Fig. 9d). This is in agreement with the detection of $LaBO_3$, SrB_2O_4 and Mn_2O_3 on the surface of the boron poisoned LSM bar sample by XRD.[26] The NanoSIMS results clearly indicate that boron deposition or reaction causes the enrichment and/or segregation of La and Mn at the electrode/electrolyte interface region.

The deposition of boron species in the LSM cathodes was also confirmed by ICP-OES. After polarization in the presence of borosilicate glass for 20 h, 0.12 wt% boron was deposited. The boron concentration increased to 0.24 wt% when the polarization was prolonged to 100 h. This is much higher than the boron content of ∼500 ppm in the LSCF electrode and ∼40 ppm in the LSM-YSZ electrode after the cell test at a boron partial pressure of $\sim 10^{-9}$ atm at 750°C for 150 h.[2] The significantly high deposition of boron confirms the effectiveness of the specifically designed borosilicate glass test arrangement as shown in Scheme 1b for the accelerated boron deposition and poisoning process on the electrochemical activity of LSM electrode.

Fig. 10 shows the XPS results on the outer surface of LSM electrodes after polarization at 200 mA cm^{-2} for 100 h as well as after

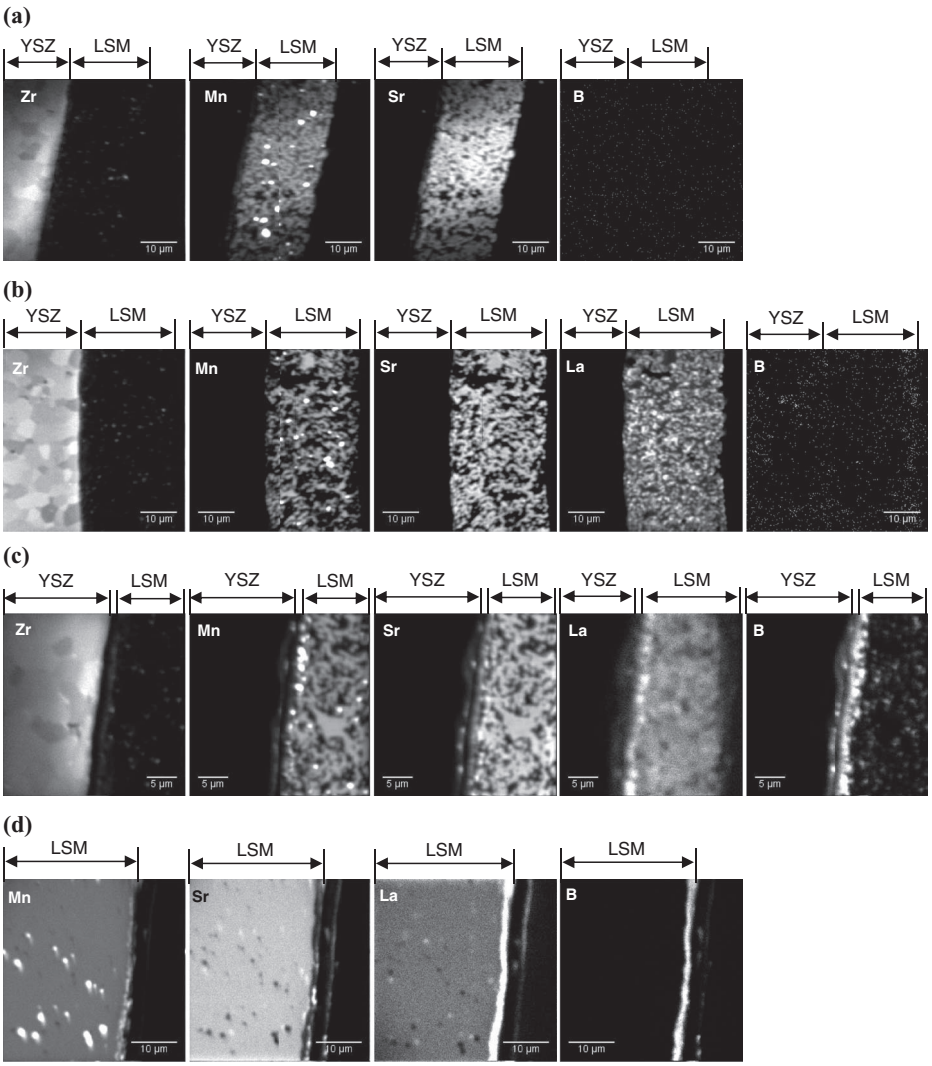

Figure 9. NanoSIMS images of cross sections of LSM cathodes: (a) as-prepared, and after the cathodic current passage at 200 mA cm^{-2} and 800°C for 100 h in the (b) absence and (c) presence of borosilicate glass. NanoSIMS images of a LSM bar sample after heat-treatment at 800°C in the presence of borosilicate glass for 30 days are shown in (d).

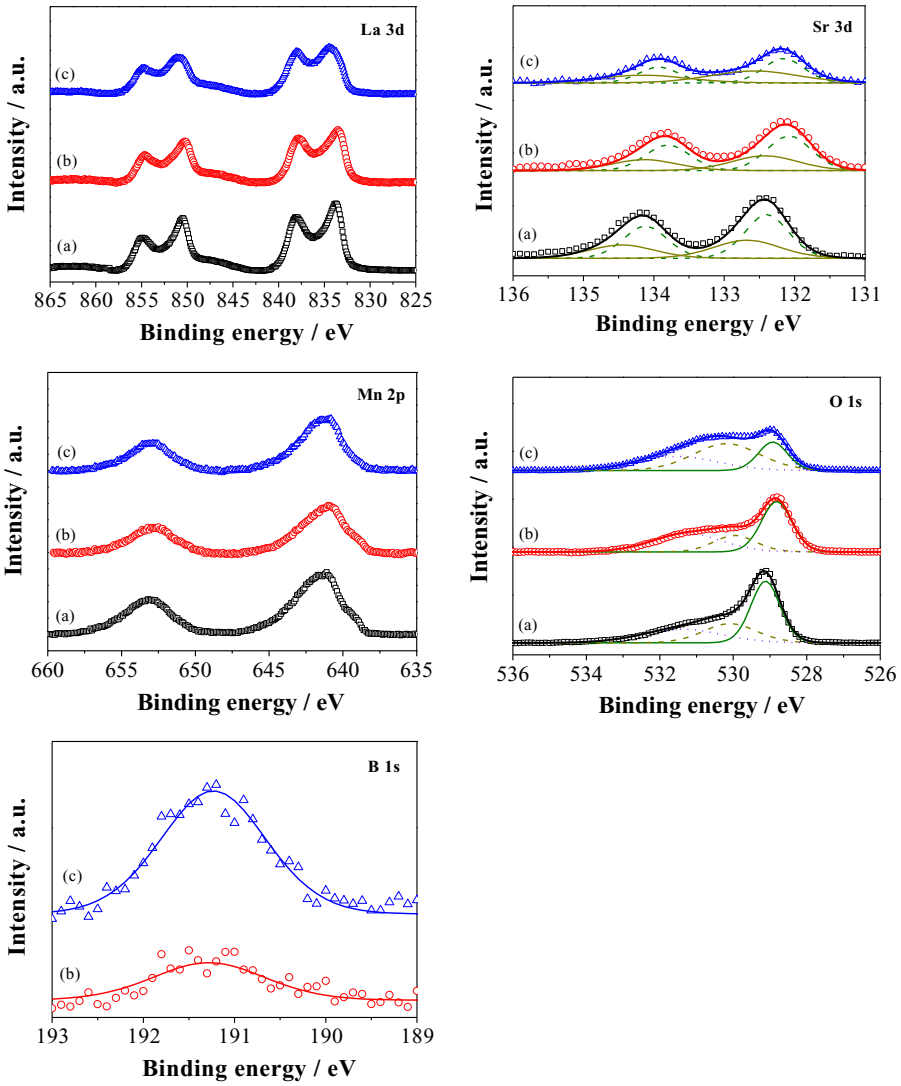

Figure 10. La3d, Sr3d, Mn2p, O1s and B1s core levels XPS spectra on outer surface of LSM electrodes: (a) as-prepared, (b) after the cathodic current passage at 200 mA cm^{-2} and 800°C for 100 h, and (c) under open circuit at 800°C for 20 h.

operation under open circuit conditions for 20 h. The detailed binding energy and element ratio are shown in Table I. After the operation in the presence of borosilicate glass, a B1s peak occurred at a binding energy of 191.2 eV on the electrode surface. The same binding energy was also observed in $LaCa_4O(BO_3)_3$,[35] lower than 193.1 eV of B_2O_3 and 192.8 eV of H_3BO_3.[36] This indicates that the detected boron most likely originates from borates. The B1s signal intensity under the open circuit conditions is much higher than that under the cathodic polarization, consistent with the SEM observation of less boron deposition on the electrode surface under the influence of cathodic polarization as compared to that under open circuit (Figs. 3 and 4).

For the samples tested in the presence of borosilicate glass, La, Sr, Mn and O experience negligible changes after the polarization for 100 h, while the operation under open circuit conditions for 20 h results in a distinct shift of La3d peak and changes in the ratio of Sr3d and O1s. The O1s signal consists of a main peak associated with the lattice oxygen and a broad shoulder related to the adsorbed oxygen species such as water, hydroxyl groups and/or carbonate.[37–39] After the test under open circuit in the presence of borosilicate glass, the surface oxygen species accounted for 78% of the total oxygen, higher than 54% of the as-prepared LSM. In the case of Sr3d states, the as-prepared LSM has two Sr components with $3d_{5/2}$ binding energy of 132.4 and

Table I. Summary of binding energies (BE) and element ratio determined by XPS on the outer surface of LSM cathodes.

		As prepared		After cathodic polarization, 100 h		After open circuit, 20 h	
Peaks		BE/eV	Element ratio/%	BE/eV	Element ratio/%	BE/eV	Element ratio/%
La $3d_{5/2}$/eV	Main	833.7	-	833.5	-	834.5	-
	Satellite	838.2	-	837.8	-	838.0	-
	Gap	4.5	-	4.2	-	3.5	-
Sr $3d_{5/2}$/eV		132.4	61.5	132.1	61.3	132.2	48.4
		132.7	38.5	132.4	38.7	132.6	51.6
Mn $2p_{3/2}$/eV		641.1	-	641.0	-	641.1	-
O 1s/eV		529.1	46.0	528.8	43.8	528.9	22.1
		530.1	26.0	530.0	19.9	530.2	47.3
		531.4	28.0	531.3	36.3	531.5	30.6
B 1s/eV		-	-	191.3	-	191.2	-

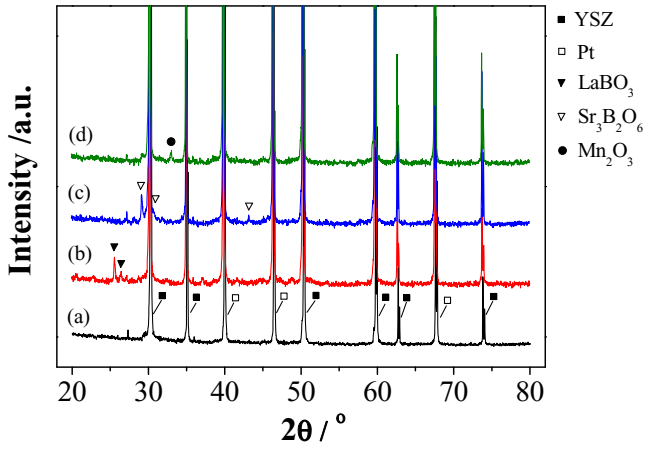

Figure 11. XRD patterns of (a) a Pt electrode, and infiltrated (b) $LaBO_3$-Pt, (c) $Sr_3B_2O_6$-Pt and (d) Mn_2O_3-Pt electrodes.

132.7 eV, which are assigned to Sr in the LSM lattice and on the LSM surface such as $SrCO_3$,[37,38,40] respectively. After the test under open circuit, the $Sr3d_{5/2}$ binding energies remain almost unchanged, but the amount of strontium species on the surface increased from 39% of the as-prepared LSM electrode to 52% after the test for 20 h. The $La3d_{5/2}$ XPS signal of the as-prepared LSM consists of a main peak at 833.7 eV and a satellite peak at 838.2 eV, and the energy gap between the two peaks is 4.5 eV. The test under open circuit in the presence of borosilicate glass gives rise to a 0.8 eV shift of the main peak toward higher binding energy and a decrease of the energy gap to 3.5 eV, lower than 4.0 eV of La_2O_3.[36,37] This indicates that after the test under open circuit the La3d signal is most likely not from the LSM lattice. Therefore taking into account the existence of distinct B1s signal from borates and the significant shift of La3d peaks, fine deposits on the LSM electrode surface after the test under open circuit conditions (Fig. 4c) are most likely the $LaBO_3$ particles.

Electrocatalytic activity of the reaction products.— To understand the inhibition effect of boron deposition on the electrocatalytic activity of LSM, we used a well-defined thin Pt electrode as the model skeleton to load 0.2 mg cm^{-2} lanthanum borate, strontium borate and manganese oxide. XRD confirmed the formation of $LaBO_3$, $Sr_3B_2O_6$ and Mn_2O_3 in the Pt skeletons (Fig. 11). Figure 12 shows the impedance responses of pristine Pt and infiltrated Pt electrodes at 800°C and plots of R_E as a function of temperature. The $LaBO_3$ and in particular $Sr_3B_2O_6$ infiltrated Pt electrodes show very poor electrocatalytic activities (Fig. 12a) and the R_E increases quickly with decreasing the temperature (Fig. 12b). The poor electrode activity is due to the electrochemical inertness of the borates for the O_2 reduction reaction. On the other hand, the Mn_2O_3 infiltration dramatically enhances the O_2 reduction reaction on the Pt electrode. R_E of the pristine Pt electrode was 11.6 Ω cm^2 at 800°C, and decreased substantially to 0.67 Ω cm^2 for the Mn_2O_3 infiltrated Pt. Hibino et al. also reported that the addition of MnO_2 significantly promoted the electrocatalytic activities of Au and Pt electrodes of single-chamber SOFC.[41] However, the significant poisoning effect of boron species on the electrocatalytic activity of LSM electrodes (Fig. 1b) clearly indicates that the negative effect of the borates formation overrides the positive effect of forming the Mn_2O_3 nanoparticles/clusters at the electrode/electrolyte interface region.

Reaction between boron and lanthanum in LSM lattice.— Strontium surface segregation under the operation conditions of SOFCs is well known for the LSM electrodes.[42–46] One of the main driving forces for the Sr segregation is the size mismatch due to the larger ionic radius of cation dopant Sr^{2+} than the host cation La^{3+}. The large Sr^{2+} is under a compressive strain/stress state in the bulk, which can be relaxed when it moves to the surface, resulting in the migration and formation of SrO species on the surface of related perovskite oxides.[47–50] However, the present study shows that in the case of open circuit operation conditions in the presence of borosilicate glass, $LaBO_3$ rather than strontium borate is formed on the LSM grain surface, as shown by the XPS analysis (Figs. 4 and 10), consistent with previous studies.[22] This indicates that gaseous boron species is highly active with La rather than surface segregated Sr. As there have been no reports or evidences on the lanthanum segregation on lanthanum strontium perovskites, the reaction must take place between the boron species and La in the LSM lattice sites. This explains random deposition/formation of $LaBO_3$ fine particles on the LSM surface under open circuit (Fig. 4). The isolated deposition of fine particles at the electrode/electrolyte interface (indicated by the circle, Fig. 4a) is most likely due to the interaction between the boron species and the minor $La_2Zr_2O_7$ phase formed on the YSZ electrolyte surface during the electrode sintering process at high temperatures.[51] Thus, under the open circuit condition, the early stage of the boron deposition and reaction can be expressed by:

$$La_{0.8}Sr_{0.2}MnO_3 + xBO_2 \rightarrow La_{0.8-x}Sr_{0.2}MnO_{3-1.5x} + xLaBO_3 \quad [1]$$

Under the cathodic polarization, the boron deposition and reaction is predominantly at the electrode/electrolyte interface region (Figs. 3 and 9). The preferential boron deposition and reaction indicate that the LSM phase at the electrode/electrolyte interface region during the O_2 reduction reaction would become more active and energetic in comparison with the LSM in the electrode bulk or on the electrode surface. This may be attributed to the effect of oxygen vacancy formation at the interface under the cathodic polarization as LSM is essentially electronic conductor with negligible oxygen ionic conductivity.[52] Computational studies showed that oxygen vacancies tend to be created on the LSM surface under the SOFC operational conditions due to the significantly reduced formation energy,[53,54] while the high cathodic polarization enhances the formation of oxygen vacancies at the electrode/electrolyte interface.[31,55–57] The presence of

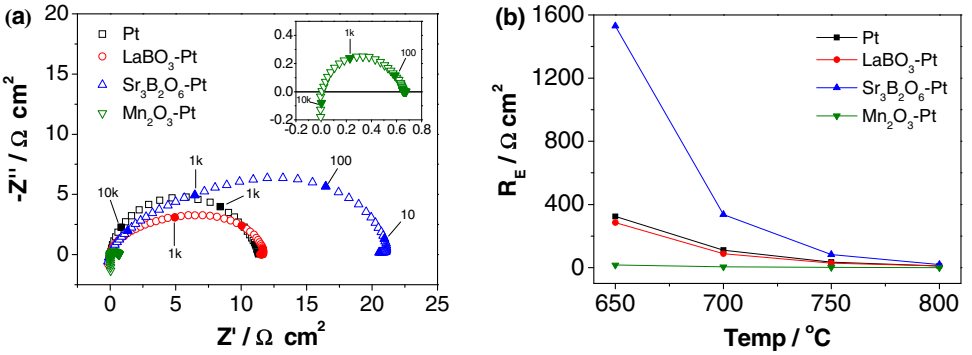

Figure 12. (a) Impedance responses and (b) plots of R_E as a function of temperature for Pt and $LaBO_3$, $Sr_3B_2O_6$ and Mn_2O_3 infiltrated Pt electrodes.

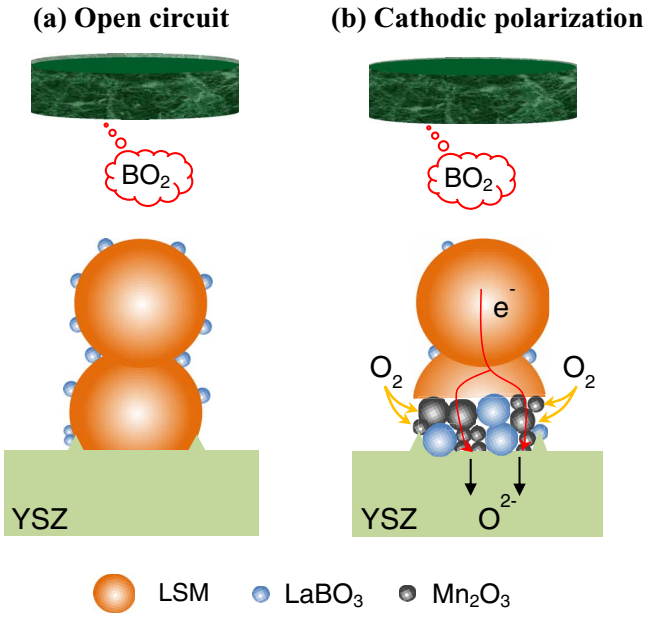

Figure 13. Schemes of the boron deposition in the LSM electrodes (a) under open circuit and (b) under cathodic polarization conditions.

positively charged oxygen vacancies would make the surrounding atoms polarized toward the vacancies.[54] In the case of mixed ionic and electronic conductor (Ba,Sr)(Co,Fe)$O_{3-\delta}$ (BSCF), the presence of highly concentrated oxygen vacancies can result in a local lattice perturbation and a local charge redistribution, as well as expansion of the lattice volume.[58] The active and energetic LSM lattice at the electrode/electrolyte interface or three phase boundary (tpb) regions is also supported by the observed crystal facet formation on the LSM grains in direct contact with YSZ electrolyte (Fig. 3c). Thus, under the cathodic polarization, the boron deposition is driven to the interface region due to the increased activity of La at the LSM lattice sites. The significant extraction of lattice La will lead to the complete decomposition of LSM perovskite at the electrode/electrolyte interface region, forming $LaBO_3$ and Mn_2O_3 nanoparticles as shown by FIB-SEM and NanoSIMS results (Figs. 7–9). The increased energy and activity induced reaction and decomposition of LSM at tpb can be written as follows:

$$La_{0.8}Sr_{0.2}MnO_{3,tpb} \xrightarrow{Cathodic\ polarization} La_{0.8}Sr_{0.2}MnO_{3,tpb}\uparrow \quad [2]$$

$$La_{0.8}Sr_{0.2}MnO_{3,tpb}\uparrow + (0.8+0.2y)\,BO_2 \rightarrow 0.8LaBO_3 + 0.2SrB_yO_z + 0.5Mn_2O_3 + (0.35+0.2y-0.1z)\,O_2 \quad [3]$$

In the reaction, $La_{0.8}Sr_{0.2}MnO_3\uparrow$ indicates the energetic and active state of LSM at the interface under cathodic polarization. Fig. 13 illustrates schematically the boron deposition under open circuit and cathodic polarization conditions. Under the open circuit conditions, the boron deposition and the formation of $LaBO_3$ is random, and some isolated deposition of catalytically inert borates at the three phase boundaries would also occur due to the minor $La_2Zr_2O_7$ phase (Fig. 13a). Under the cathodic polarization, the interaction between boron species and energetic lattice La is accelerated and Reaction 3 becomes dominant due to the significant shift of Reaction 1 to the right. The deterioration of the electrode/electrolyte interface and formation of electrochemically inert $LaBO_3$ phase retards the O_2 reduction reaction and degrades both the electrochemical activity and microstructure of the LSM electrodes.

The present studies show the potential detrimental effect of volatile boron species on the electrocatalytic activity and long-term stability of lanthanum based perovskite cathodes of SOFCs. However, the volatility of borosilicate based glass sealants can be effectively depressed by optimization of the glass composition and by the effective stack design to minimize the exposed areas of glass sealant to the air stream. For example, addition of Bi_2O_3 can inhibit the formation of $LaBO_3$ between borosilicate and lanthanum strontium cobalt ferrite (LSCF) cathode and enhances the [BO_3] to [BO_4] transition in glass structure, improving the thermal stability of boron species in glass matrix.[11] Development of borosilicate glass with low boron volatility or boron-free glass-based sealants is also effective to eliminate the adverse effect of boron deposition and poisoning.[10,23]

Conclusions

Boron deposition and poisoning of the LSM cathodes was studied under the accelerated SOFC operation conditions. Boron deposition on the surface of LSM electrode is essentially random under open circuit conditions, but is driven to the electrode/electrolyte interface region under the cathodic polarization conditions. The results indicate that boron is highly reactive with the lattice La ions in the LSM perovskite structure to form thermodynamically stable and electrochemically inert $LaBO_3$, causing La enrichment and segregation. The kinetics of the reaction is closely dependent on the activity of La ions. As LSM is a predominant electronic conductor with negligible oxygen ionic conductivity, the O_2 reduction reaction mainly occurs at the electrode/electrolyte interface; this in turn results in the highly active and energetic lattice La in the LSM perovskite structure and thus accelerates the reaction with the boron species. The extraction of La from the LSM causes the structural destruction of LSM perovskite phase, forming $LaBO_3$ and Mn_2O_3 and substantially degrades the electrochemical activity and stability of LSM electrodes for the O_2 reduction reaction.

Acknowledgments

The project is supported by Curtin University Research Fellow Program. The authors thank the technical assistance of Dr Kane O'Donnell on XPS analysis and acknowledge the facilities, scientific and technical assistance of the Curtin University Microscopy & Microanalysis Facility, the Australian Microscopy & Microanalysis Research Facility at the Centre for Microscopy, Characterisation & Analysis, The University of Western Australia, both of which are partially funded by the University, State and Commonwealth Governments, and the WA X-Ray Surface Analysis Facility, funded by the Australian Research Council LIEF grant (LE120100026).

References

1. Y. P. Xiong, K. Yamaji, T. Horita, H. Yokokawa, J. Akikusa, H. Eto, and T. Inagaki, *J. Electrochem. Soc.*, **156**, B588 (2009).
2. X. D. Zhou, J. W. Templeton, Z. Zhu, Y. S. Chou, G. D. Maupin, Z. Lu, R. K. Brow, and J. W. Stevenson, *Journal of the Electrochemical Society*, **157**, B1019 (2010).
3. S. P. Jiang and X. Chen, *International Journal of Hydrogen Energy*, **39**, 505 (2014).
4. J. W. Fergus, *Journal of Power Sources*, **147**, 46 (2005).
5. M. K. Mahapatra and K. Lu, *Materials Science & Engineering R-Reports*, **67**, 65 (2010).
6. N. H. Menzler, P. Batfalsky, S. Groß, V. Shemet, and F. Tietz, *ECS Transactions*, **35**, 195 (2011).
7. Y.-S. Chou, J. W. Stevenson, and J.-P. Choi, *Journal of Power Sources*, **250**, 166 (2014).
8. J. L. Chen, H. W. Yang, R. Chadeyron, D. Tang, and T. Zhang, *J. Eur. Ceram. Soc.*, **34**, 1989 (2014).
9. Q. Zhang, H. W. Yang, F. R. Zeng, S. R. Wang, D. Tang, and T. Zhang, *Rsc Advances*, **5**, 41772 (2015).
10. F. Smeacetto, M. Salvo, M. Santarelli, P. Leone, G. A. Ortigoza-Villalba, A. Lanzini, L. C. Ajitdoss, and M. Ferraris, *Int. J. Hydrog. Energy*, **38**, 588 (2013).
11. L. H. Fang, H. L. Liu, D. D. Zhao, H. W. Yang, D. Tang, and T. Zhang, *J. Eur. Ceram. Soc.*, **34**, 4463 (2014).
12. L. H. Fang, Q. Zhang, F. Lin, D. Tang, and T. Zhang, *J. Eur. Ceram. Soc.*, **35**, 2201 (2015).
13. B. Dev and M. E. Walter, *J. Fuel Cell Sci. Technol.*, **12** (2015).
14. C. K. Lin, Y. A. Liu, S. H. Wu, C. K. Liu, and R. Y. Lee, *J. Power Sources*, **280**, 272 (2015).
15. T. Zhang, W. G. Fahrenholtz, S. T. Reis, and R. K. Brow, *J. Am. Ceram. Soc.*, **91**, 2564 (2008).

16. S. P. Jiang, L. Christiansen, B. Hughan, and K. Foger, *J. Mater. Sci. Lett.*, **20**, 695 (2001).
17. T. Komatsu, K. Watanabe, M. Arakawa, and H. Arai, *Journal of Power Sources*, **193**, 585 (2009).
18. K. Chen, N. Ai, C. Lievens, J. Love, and S. P. Jiang, *Electrochemistry Communications*, **23**, 129 (2012).
19. K. Chen, N. Ai, L. Zhao, and S. P. Jiang, *Journal of the Electrochemical Society*, **160**, F183 (2013).
20. K. Chen, N. Ai, L. Zhao, and S. P. Jiang, *Journal of the Electrochemical Society*, **160**, F301 (2013).
21. K. Chen, J. Hyodo, K. M. O'Donnell, W. Rickard, T. Ishihara, and S. P. Jiang, *Journal of The Electrochemical Society*, **161**, F1163 (2014).
22. K. Chen, N. Ai, and S. P. Jiang, *Fuel Cells*, **13**, 1101 (2013).
23. K. F. Chen, L. H. Fang, T. Zhang, and S. P. Jiang, *Journal of Materials Chemistry A*, **2**, 18655 (2014).
24. S. P. Jiang, J. P. Zhang, L. Apateanu, and K. Foger, *J. Electrochem. Soc.*, **147**, 4013 (2000).
25. T. Zhang and Q. Zou, *Journal of the European Ceramic Society*, **32**, 4009 (2012).
26. K. Chen, J. Hyodo, L. Zhao, N. Ai, T. Ishihara, and S. P. Jiang, *Journal of the Electrochemical Society*, **160**, F1033 (2013).
27. N. Ai, K. Chen, and S. P. Jiang, *Solid State Ionics*, **233**, 87 (2013).
28. S. P. Jiang, *J. Solid State Electrochem.*, **11**, 93 (2007).
29. S. P. Jiang, J. P. Zhang, and K. Foger, *J. Electrochem. Soc.*, **147**, 3195 (2000).
30. S. P. Jiang, *Solid State Ionics*, **146**, 1 (2002).
31. S. P. Jiang and W. Wang, *Electrochem. Solid State Lett.*, **8**, A115 (2005).
32. D. L. Meixner and R. A. Cutler, *Solid State Ionics*, **146**, 273 (2002).
33. T.-Z. Ren, Z.-Y. Yuan, W. Hu, and X. Zou, *Microporous and Mesoporous Materials*, **112**, 467 (2008).
34. M. Sasidharan, N. Gunawardhana, H. N. Luitel, T. Yokoi, M. Inoue, S.-i. Yusa, T. Watari, M. Yoshio, T. Tatsumi, and K. Nakashima, *Journal of Colloid and Interface Science*, **370**, 51 (2012).
35. A. J. Nelson, T. van Buuren, T. M. Willey, C. Bostedt, J. J. Adams, K. I. Schaffers, L. Terminello, and T. A. Callcott, *Journal of Electron Spectroscopy and Related Phenomena*, **137–140**, 541 (2004).
36. C. Wagner, W. Riggs, L. Davis, J. Moulder, and G. Muilenberg, *Handbook of X-ray Photoelectron Spectroscopy; Perkin-Elmer Corporation: Eden Prairie, MN*, 74 (1979).
37. C. C. Kan and E. D. Wachsman, *J. Electrochem. Soc.*, **156**, B695 (2009).
38. C. Knöfel, H.-J. Wang, K. T. S. Thydén, and M. Mogensen, *Solid State Ionics*, **195**, 36 (2011).
39. W. Wang, H.-b. Zhang, G.-d. Lin, and Z.-t. Xiong, *Applied Catalysis B: Environmental*, **24**, 219 (2000).
40. Q.-H. Wu, M. Liu, and W. Jaegermann, *Materials Letters*, **59**, 1980 (2005).
41. T. Hibino, Y. Kuwahara, and S. Wang, *Journal of The Electrochemical Society*, **146**, 2821 (1999).
42. S. P. Jiang and J. G. Love, *Solid State Ionics*, **138**, 183 (2001).
43. N. Caillol, M. Pijolat, and E. Siebert, *Appl. Surf. Sci.*, **253**, 4641 (2007).
44. T. T. Fister, D. D. Fong, J. A. Eastman, P. M. Baldo, M. J. Highland, P. H. Fuoss, K. R. Balasubramaniam, J. C. Meador, and P. A. Salvador, *Applied Physics Letters*, **93** (2008).
45. H. Jalili, J. W. Han, Y. Kuru, Z. H. Cai, and B. Yildiz, *Journal of Physical Chemistry Letters*, **2**, 801 (2011).
46. A.-K. Huber, M. Falk, M. Rohnke, M. Luer, L. Gregoratti, M. Amati, and J. Janek, *Physical Chemistry Chemical Physics*, **14**, 751 (2012).
47. S. P. Jiang, *J. Mater. Sci.*, **43**, 6799 (2008).
48. H. P. Ding, A. V. Virkar, M. L. Liu, and F. Liu, *Phys. Chem. Chem. Phys.*, **15**, 489 (2013).
49. L. Zhao, J. Drennan, C. Kong, S. Amarasinghe, and S. P. Jiang, *Journal of Materials Chemistry A*, **2**, 11114 (2014).
50. D. Oh, D. Gostovic, and E. D. Wachsman, *J. Mater. Res.*, **27**, 1992 (2012).
51. K. Chen, J. Hyodo, A. Dodd, N. Ai, T. Ishihara, J. Li, and S. P. Jiang, *Faraday Discussions*, in press (2015).
52. R. J. Chater, S. Carter, J. A. Kilner, and B. C. H. Steele, *Solid State Ionics*, **53**, 859 (1992).
53. Y. Choi, M. E. Lynch, M. C. Lin, and M. Liu, *The Journal of Physical Chemistry C*, **113**, 7290 (2009).
54. E. A. Kotomin, Y. A. Mastrikov, E. Heifets, and J. Maier, *Physical Chemistry Chemical Physics*, **10**, 4644 (2008).
55. T. Horita, K. Yamaji, N. Sakai, H. Yokokawa, T. Kawada, and T. Kato, *Solid State Ionics*, **127**, 55 (2000).
56. M. E. Lynch, D. Ding, W. M. Harris, J. J. Lombardo, G. J. Nelson, W. K. S. Chiu, and M. L. Liu, *Nano Energy*, **2**, 105 (2013).
57. S. S. Nonnenmann, R. Kungas, J. Vohs, and D. A. Bonnell, *ACS Nano*, **7**, 6330 (2013).
58. Y. A. Mastrikov, M. M. Kuklja, E. A. Kotomin, and J. Maier, *Energy & Environmental Science*, **3**, 1544 (2010).